Research Square

Preprints are preliminary reports that have not undergone peer review.
They should not be considered conclusive, used to inform clinical practice,
or referenced by the media as validated information.

A near-quantum-limited diamond maser amplifier operating at millikelvin temperatures

Yuimaru Kubo

yuimaru.kubo@oist.jp

Okinawa Institute of Science and Technology Graduate University https://orcid.org/0000-0001-5803-4287

Morihiro Ohta

Okinawa Institute of Science and Technology Graduate University

Ching-Ping Lee

Department of Physics, National Tsing Hua University

Vincent Sietses

QuTech and Kavli Institute of Nanoscience, Delft University of Technology

Ivan Kostylev

Okinawa Institute of Science and Technology Graduate University https://orcid.org/0000-0003-2975-0027

Jason Ball

Liquid Instruments https://orcid.org/0000-0003-2311-1355

Petr Moroshkin

School of Engineering, Brown University

Tatsuki Hamamoto

Okinawa Institute of Science and Technology Graduate University https://orcid.org/0000-0002-8654-9322

Yutaka Kobayashi

Sumitomo Electric Industries Ltd.

Shinobu Onoda

National Institutes for Quantum Science and Technology https://orcid.org/0000-0003-1425-0708

Takeshi Ohshima

National Institutes for Quantum Science and Technology (QST) https://orcid.org/0000-0002-7850-3164

Junichi Isoya

University of Tsukuba https://orcid.org/0000-0002-9598-625X

Hiroki Takahashi

Okinawa Institute of Science and Technology

Physical Sciences - Article

Keywords:

Posted Date: June 20th, 2025

DOI: https://doi.org/10.21203/rs.3.rs-6766240/v1

License: This work is licensed under a Creative Commons Attribution 4.0 International License.
Read Full License

Additional Declarations: There is **NO** Competing Interest.

Version of Record: A version of this preprint was published at Nature Communications on November 16th, 2026. See the published version at https://doi.org/10.1038/s41467-026-79021-7.

A near-quantum-limited diamond maser amplifier operating at millikelvin temperatures

Morihiro Ohta[1†], Ching-Ping Lee[2,8†], Vincent P.M. Sietses[1,9], I. Kostylev[2], J.R. Ball[3,10], P. Moroshkin[3,11], T. Hamamoto[1], Y. Kobayashi[4], S. Onoda[5], T. Ohshima[5,6], J. Isoya[7], Hiroki Takahashi[1], Yuimaru Kubo[2*]

[1]Experimental Quantum Information Physics Unit, Okinawa Institute of Science and Technology Graduate University, Onna, Okinawa, 904-0495, Japan.
[2]The Science and Technology Group, Okinawa Institute of Science and Technology Graduate University, Onna, Okinawa, 904-0495, Japan.
[3]Quantum Dynamics Unit, Okinawa Institute of Science and Technology Graduate University, Onna, Okinawa, 904-0495, Japan.
[4]Sumitomo Electric Industries Ltd., Itami, Hyogo, 664-0016, Japan.
[5]Quantum Materials and Applications Research Center, Takasaki Institute for Advanced Quantum Science, National Institutes for Quantum Science and Technology, Takasaki, Gunma, 370-1292, Japan.
[6]Department of Materials Science, Tohoku University, Sendai, Miyagi, 980-8579, Japan.
[7]Graduate School of Pure and Applied Sciences, University of Tsukuba, Tsukuba, Ibaraki, 305-8550, Japan.
[8]Present address: Department of Physics, National Tsing Hua University, Hsinchu, 30013, Taiwan.
[9]Present address: QuTech and Kavli Institute of Nanoscience, Delft University of Technology, Delft, 2600 GA, Netherlands.
[10]Present address:, Liquid Instruments, San Diego, CA, 92130, USA.
[11]Present address: School of Engineering, Brown University, Providence, RI, 02912, USA.

*Corresponding author(s). E-mail(s): yuimaru.kubo@oist.jp;
†These authors contributed equally to this work.

Abstract

The tremendous progress in detecting tiny microwave signals from quantum devices under test at millikelvin temperatures has been enabled by superconducting parametric amplifiers [1–4], owing to their near-quantum-limited noise performance [5, 6]. Another fundamentally distinct approach could be offered by masers, the microwave counterpart of lasers, which have long been predicted to exhibit quantum-limited noise performance when operated in the absence of thermal noise and with sufficient population inversion [7–11]. Here, we demonstrate the first-ever non-superconducting, near-quantum-limited microwave amplifier operating at millikelvin temperatures based on a maser utilising impurity spins in diamond. We achieve power gains exceeding 30 dB, a minimum noise temperature of 0.86 K (corresponding to 2.2 noise photons), and a maximum 1 dB output compression point of −63 dBm at 6.595 GHz. The observed noise temperature is on par with superconducting parametric amplifiers, while the compression points exceed those of Josephson travelling-wave parametric amplifiers by 20 to 30 dB. By revisiting masers at millikelvin temperatures, our work reestablishes them as robust low-noise amplifiers for emerging quantum technologies, including quantum computing, magnetic resonance spectroscopy [12, 13], and fundamental physics [14–16].

Theoretical work on masers (microwave amplification by stimulated emission of radiation) dating back to the 1950s established that they could reach quantum-limited noise under ideal conditions [7–9]. Despite this early promise, however, solid-state masers have been constrained by their dependence on cryogenic operation, which has hindered their application in classical communication technologies. Yet in the context of modern microwave quantum technologies, the cryogenic requirement is no longer a drawback.

Diamond masers, particularly those based on negatively charged nitrogen-vacancy (NV^-) centres, have emerged as both oscillators [10, 17] and amplifiers at room temperature [11] and cryogenic temperatures [18]. In addition, cavity cooling [11, 19, 20] and enhanced magnetometry [21] at room temperature have been demonstrated, suggesting the potential of diamond-based masers as resources for microwave quantum technology applications. However, the requirement for optical pumping to establish population inversion in NV^- centres presents a significant challenge for applications at millikelvin temperatures due to the high laser powers required and the limited cooling power of dilution refrigerators. Here we achieve population inversion in substitutional nitrogen defects (P1 centres) in diamond through microwave pumping at power levels of 100 nanowatts or less. We demonstrate amplification with near-quantum-limited noise at millikelvin temperatures.

Maser amplifier device and setup

Figure 1a illustrates the maser amplifier device. It consists of a loop-gap microwave resonator [22] that houses a diamond crystal containing approximately 16 ppm of P1 centres, together with about 2 ppm of negatively-charged nitrogen-vacancy (NV^-) centres [22, 23], with dimensions of $3 \times 1.5 \times 0.5\,\mathrm{mm}^3$. The resonator's frequency is $\omega_r/2\pi \approx 6.595\,\mathrm{GHz}$ and its internal quality factor is $Q_{\mathrm{int}} \approx 3000$. In this work, we operate the resonator with two different external quality factors, $Q_{\mathrm{ext}} \approx 250$ and ≈ 730, by adjusting the number of turns of the coupling loop antenna.

Figure 1b illustrates a simplified measurement setup inside the refrigerator. The maser amplifier device is thermalised to the mixing chamber plate at 13 mK in a dilution refrigerator. Two microwave input lines, one heavily attenuated for the probe and another moderately attenuated for the pump, are combined through a directional coupler. After being combined, the pump and probe microwave tones go to the maser amplifier device through a circulator, which in turn directs the reflected signal to the measurement line and decouples the thermal noise from the following HEMT (high electron mobility transistor) amplifier placed at the 4 K stage. An impedance-matched temperature-variable noise source [24] is integrated along the probe line, which is weakly thermalised to the cold plate at approximately 100 mK. We use this noise source to characterise the noise temperature of our diamond maser amplifier.

Operating principle

The electron spins of the P1 centres are the active medium in our maser amplifier. These centres possess an electron spin $S = 1/2$ and a nuclear spin $I = 1$, with a hyperfine interaction tensor characterised by $\mathcal{A}_\perp/2\pi = 81.33\,\mathrm{MHz}$ and $\mathcal{A}_{||}/2\pi = 114.03\,\mathrm{MHz}$. Under a static magnetic field aligned parallel to the cubic crystallographic axis [001] of the diamond, the electron spin states ($S = \pm\frac{1}{2}$) split into three levels depending on the nuclear spin states, $\mathrm{P1}_+$, $\mathrm{P1}_0$, and $\mathrm{P1}_-$, as shown in Fig. 2a. The corresponding transition frequencies, denoted as ω_+, ω_0, and ω_-, satisfy an energy conserving relationship $2\omega_0 = \omega_- + \omega_+$, which facilitates a four-spin cross-relaxation process between the central transition ($m_I = 0$) and the two satellite transitions ($m_I = \pm 1$) [25–27].

The operating principle of our maser amplifier is described in Figs. 2b, c, d, and e. First, we apply a static magnetic field B_{DC} to align the frequency ω_+ with the resonator frequency ω_r, and then pump the $\mathrm{P1}_0$ transition at ω_0 with a rate Γ_{p}, as illustrated in Fig. 2b. This pumping triggers the excitation of one $\mathrm{P1}_+$ and one $\mathrm{P1}_-$ spin by exchanging the energy with two $\mathrm{P1}_0$ spins through the four-spin cross-relaxation process [25, 26] at a rate of Γ_{cr}, as depicted in Fig. 2c. Ordinarily, such pumping would lead to saturation across all transitions. However, the dynamics are modified by the difference between the relaxation times of the spins in $\mathrm{P1}_-$ and $\mathrm{P1}_+$, as demonstrated in Fig. 2f, with respective values of $T_{1\text{-}} \approx 1030\,\mathrm{s}$ and $T_{1+} \approx 1650\,\mathrm{s}$. The faster relaxation of $\mathrm{P1}_-$ is induced by another "fast-relaxing" spin system, which coexists within the diamond crystal and exhibits relaxation times on the order of ten milliseconds (see inset of Fig. 2f). The transition frequencies of these "fast-relaxing" spins largely overlap with the $\mathrm{P1}_-$ transition around ω_-, thereby accelerating the relaxation of

the $P1_-$ spins through magnetic dipole-dipole interactions, as indicated by $\Gamma^{\text{eff}}_{P1_-}$ in Fig. 2d. This imbalance in relaxation times prevents saturation and maintains continuous excitation of the $P1_+$ state, resulting in population inversion. Although the exact nature of these fast-relaxing spins remains unidentified, they might be either neutrally-charged nitrogen-vacancy (NV^0) centres [28, 29] or nickel centres [30]. We refer to them as "fast-relaxing spins" throughout this paper.

Gain and bandwidth

Figure 3a shows the time evolution of the inverted spin population $\Delta N_{P1_+} = N^u_{P1_+} - N^l_{P1_+}$, between the upper ($u$) and lower ($l$) levels of $P1_+$ transition, extracted from the measured reflection coefficients (Methods). Above a pump power of $-58\,\text{dBm}$ at the device input, ΔN_{P1_+} becomes positive, indicating population inversion. We also simulate the dynamics using rate equations that include all P1 states and their interactions (Methods), which are shown by the solid curves in Fig. 3a. The same experiments were also performed with $Q_{\text{ext}} \approx 730$, as shown in Fig. 3b, where the system reaches the self-oscillation threshold. This is visible in the saturation of the population at $\Delta N_{P1_+} \approx 2.4 \times 10^{14}$, which aligns well with the calculated threshold indicated by the red dot-dashed horizontal line.

Figure 3c presents the maser gain spectra under various pump powers measured by a vector network analyser (VNA) under a static magnetic field of $B_{\text{DC}} = 232.15\,\text{mT}$. While the spectra show negative gains at weaker pump powers until $-59\,\text{dBm}$, the gain becomes positive above $-58\,\text{dBm}$. At a pump power of $-39\,\text{dBm}$, the gain exceeds 30 dB with a bandwidth of approximately 70 kHz, which results in a gain-bandwidth product of 2.8 MHz. Figure 3d shows the gain-bandwidth products versus inverted spin population ΔN_{P1_+} for both $Q_{\text{ext}} \approx 250$ and 730, whereas Fig. 3e plots the gain as a function of ΔN_{P1_+}, with theoretical gain curves shown as dashed lines. As in Fig. 3b, the onset of self-oscillation for the maser device with $Q_{\text{ext}} \approx 730$ is also evident in Fig. 3d above the gain-bandwidth product of approximately 2.5 MHz, as well as above gains of 30 dB in Fig. 3e.

Next, we demonstrate the frequency tunability of the diamond maser's gain profile by varying the external static magnetic field B_{DC}. As the transition frequencies of the P1 centres shift with B_{DC}, the maser's gain profile can also be tuned accordingly. Figure 3f shows the measured maser gain versus B_{DC}, demonstrating tunability over 10 MHz in the central gain and about 6 MHz in the full-width at half-maximum.

Noise temperature

To assess the noise performance of our maser amplifier, we measured the noise power spectrum in the presence of a weak microwave probe tone as a reference, with the maser turned on and off. The results displayed in Fig. 4a show a signal-to-noise ratio improvement of approximately 6 dB. This indicates that our maser amplifier achieves a noise level approximately four times lower than that of the following measurement line, which is dominated by the noise level of the HEMT amplifier.

To quantitatively evaluate our maser amplifier's noise temperature, we use the impedance-matched temperature-variable noise source [24]. This device enables independent control of the input noise temperature T_{in} to the maser amplifier, resulting in accurate determination of noise temperature. It is important to note that we also account for the attenuation of the lines between the noise source and the maser amplifier (Methods), as well as the insertion losses at the directional coupler and the circulator. We have independently measured these attenuations to obtain the accurate value of T_{in} (see Methods).

First, we characterised the base noise temperature of our measurement line with the maser amplifier turned off. In this configuration, the noise power after the HEMT amplifier as a function of T_{in}, detected within a bandwidth of δf_{BW}, is given by [24]

$$\frac{P_{\mathrm{out}}(T_{\mathrm{in}})}{G_{\mathrm{HEMT}} k_{\mathrm{B}} \delta f_{\mathrm{BW}}} \approx T_{\mathrm{in}} + T_{\mathrm{HEMT}}, \tag{1}$$

where G_{HEMT} and T_{HEMT} are the gain and noise temperature of the HEMT amplifier, respectively, and k_{B} is the Boltzmann constant. The results, shown in the inset of Fig. 4b, indicate that $T_{\mathrm{HEMT}} \approx 4.19(28)\,\mathrm{K}$.

Subsequently, we turned on the diamond maser amplifier and repeated the noise temperature measurements at various maser amplifier gains. In this configuration, the output noise power after the HEMT amplifier is given by

$$\frac{P_{\mathrm{out}}(T_{\mathrm{in}})}{G_{\mathrm{maser}} G_{\mathrm{HEMT}} k_{\mathrm{B}} \delta f_{\mathrm{BW}}} \approx T_{\mathrm{in}} + T_{\mathrm{maser}} + \frac{T_{\mathrm{HEMT}}}{G_{\mathrm{maser}}}. \tag{2}$$

Here, G_{maser} and T_{maser} represent the gain and noise temperature of the maser amplifier, respectively. As presented in Fig. 4b, the minimum noise temperature of the entire system is approximately $T_{\mathrm{sys}} = T_{\mathrm{maser}} + (T_{\mathrm{HEMT}}/G_{\mathrm{maser}}) \approx 0.902(3)\,\mathrm{K}$. After subtracting the contribution from T_{HEMT}, the minimum noise temperature of the diamond maser amplifier is obtained to be $T_{\mathrm{maser}} \approx 0.860(6)\,\mathrm{K}$, corresponding to approximate noise photons of $\bar{n}_{\mathrm{maser}} = \left(e^{\hbar\omega/k_B T_{\mathrm{maser}}} - 1\right)^{-1} \approx 2.2$.

The measured noise temperature T_{maser}, which is nearly three times higher than the quantum limit of $\bar{n}_{\mathrm{QL}} = 0.5$, corresponding to approximately 0.3 K in our setup, primarily results from imperfect population inversion[8, 11]. While the spins in the higher energy level amplify the incoming signal through stimulated emission, those remaining in the lower energy level absorb photons. This counteraction effectively introduces additional noise photons, quantified by $n_s = \left(e^{\hbar\omega/k_B|T_s|} - 1\right)^{-1}$, where negative spin temperature T_{s} and the inversion ratio $\rho = \Delta N_{P1_+}/(N^u_{\mathrm{P1}_+} + N^l_{\mathrm{P1}_+})$ are linked through

$$\rho = \tanh\left(\frac{\hbar\omega}{2k_{\mathrm{B}}|T_{\mathrm{s}}|}\right), \tag{3}$$

with $\hbar$ denoting the reduced Planck constant. As shown in Fig. 3a, the measured $\rho \approx 0.28$ at 20 dB gain corresponds to a noise temperature of $T_{\mathrm{maser}} \approx 0.79\,\mathrm{K}$ [11], in good agreement with the measured T_{maser}. It is important to note that the measured T_{maser} values are by no means the fundamental limits in our system; they are constrained by

the slow relaxation rate of the $P1_-$ spins, $\Gamma^{\text{eff}}_{P1_-} \approx 0.95\,\text{mHz}$, which in turn limits the effective pump rate on the $P1_+$ spins. With a slightly faster $\Gamma^{\text{eff}}_{P1_-}$ of 1.2 mHz, which could be realized by engineering a higher density of the fast-relaxing spins, the noise temperature could be reduced to $T_{\text{maser}} \approx 0.59\,\text{K}$. Additionally, improving the internal quality factor Q_{int} would further lower the maser amplifier's noise temperature. For instance, an order-of-magnitude improvement in Q_{int} to $\sim 10^4$, achievable without reducing the coupling constant g_0 by employing a dielectric resonator [17, 31, 32], could lower the noise temperature by approximately 0.1 K.

Compression point

To assess the dynamic range of our maser amplifier, we measured the 1 dB compression points at various maser amplifier gains. Figure 4c shows the amplifier gains as a function of input probe power. The output (input) 1 dB compression points ($P_{1\text{dB}}$) are measured to be approximately $-65\,\text{dBm}$ ($-85\,\text{dBm}$) at a gain of 20 dB, and approximately $-63\,\text{dBm}$ ($-73\,\text{dBm}$) at a gain of 10 dB. These measured compression points are 20 to 30 dB higher than those typically reported in Josephson travelling-wave parametric amplifiers [2, 6], but are two or three orders of magnitude lower than those achieved by state-of-the-art kinetic inductance travelling-wave parametric amplifiers [33, 34].

Conclusion

In conclusion, we demonstrated a near-quantum-limited diamond maser amplifier operating at millikelvin temperatures and achieved a noise photon level of $\bar{n}_{\text{maser}} \approx 2.2$. The noise level could be further reduced towards the quantum limit by increasing the effective pump rate via a higher density of fast-relaxing spins and by employing a resonator with a higher internal quality factor. By revisiting masers at millikelvin temperatures, our work re-establishes maser technology as a robust and low-noise alternative for microwave amplification in quantum technologies, including quantum computing, ultra-sensitive magnetic resonance spectroscopy, and fundamental physics.

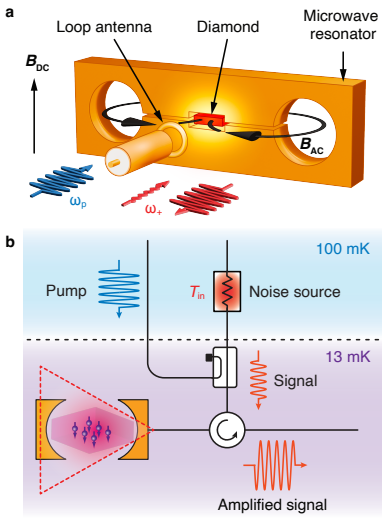


Fig. 1 Diamond maser amplifier device and setup. a, Device schematic. A diamond crystal containing P1 centres is positioned within a loop-gap microwave resonator. Both pump and probe microwave tones are introduced via a coupling loop antenna. **b**, Experimental setup at the cold plate (100 mK) and mixing chamber plate (13 mK) in a dilution refrigerator. The resonator is enclosed in a copper housing and thermalised to the mixing chamber plate. Amplified microwave signals are routed to the measurement line through a series of two circulators. Additionally, a temperature-variable noise source, weakly thermalised to 100 mK, generates input noise characterised by a temperature T_{in}.

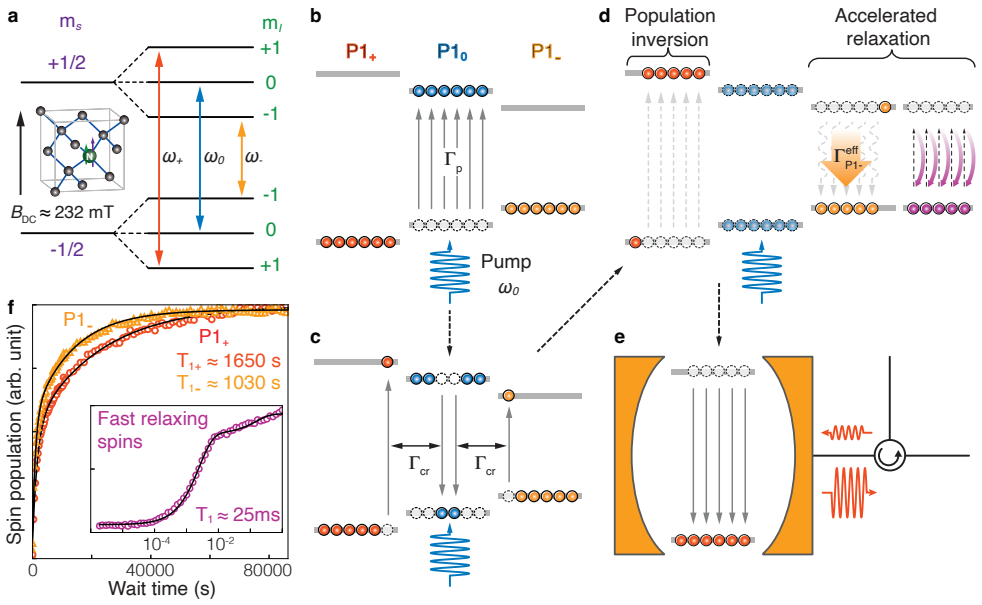


Fig. 2 Operating principle of the diamond maser amplifier. a, Illustration of a P1 centre in diamond and its energy levels under a static magnetic field of $B_{\mathrm{DC}} \approx 232\,\mathrm{mT}$, aligned parallel to the [001] crystallographic axis. **b**,**c**,**d**,**e**, System dynamics with a pump. **b**, A microwave pump tone at ω_0 excites $\mathrm{P1}_0$ spins at a rate of Γ_{p}. **c**, This pump induces the excitation of one $\mathrm{P1}_+$ and one $\mathrm{P1}_-$ spin by exchanging the energy with two $\mathrm{P1}_0$ spins at a rate of Γ_{cr} via four-spin cross-relaxation. **d**, Most $\mathrm{P1}_-$ spins quickly deplete to the lower energy state due to the "fast-relaxing spins" (detailed further in **f**). Consequently, only $\mathrm{P1}_+$ spins progressively accumulate in the higher energy state, culminating in population inversion in the $\mathrm{P1}_+$ transition. **e**, The inverted $\mathrm{P1}_+$ state amplifies the input microwave probe tone through stimulated emission. **f**, Asymmetry in energy relaxation times between $\mathrm{P1}_+$ and $\mathrm{P1}_-$, indicating a faster decay in $\mathrm{P1}_-$. The inset shows the energy relaxation of the "fast-relaxing spins" on a timescale of approximately ten milliseconds. While the data in the main panel were extracted from reflection spectroscopy measurements, those in the inset were obtained using a saturation recovery pulse sequence (see Supplementary Information section 2).

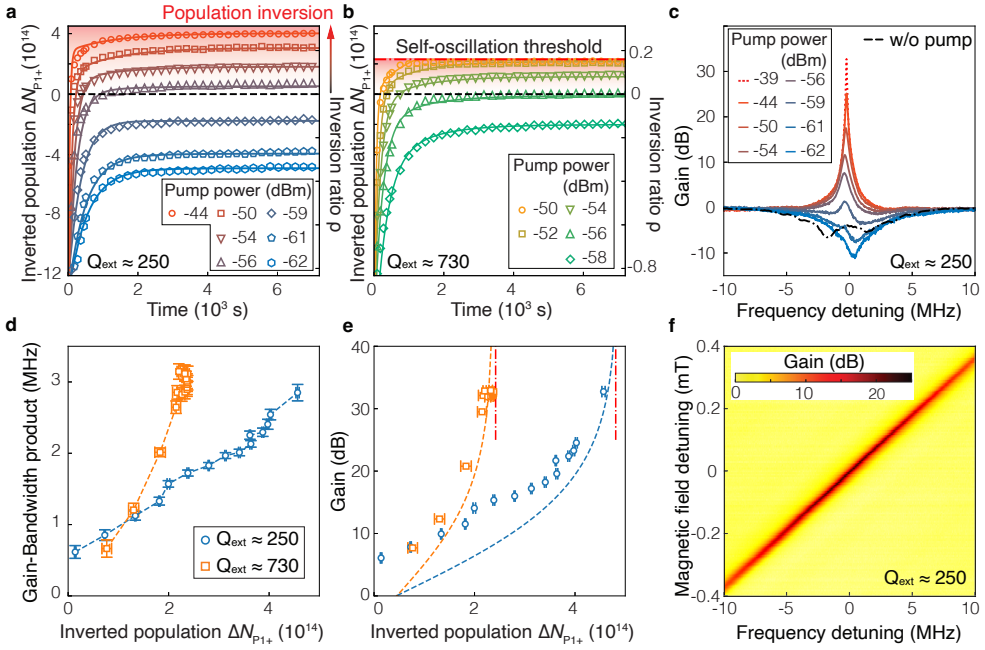


Fig. 3 Maser amplifier's gain and bandwidth. a,**b**, Inverted spin population ΔN_{P1_+} between the lower and upper $\mathrm{P1}_+$ states over time under various pump powers for two external quality factors of $Q_{\mathrm{ext}} \approx 250$ (**a**) and ≈ 730 (**b**). Open symbols represent the experimental data, while solid curves represent simulations. The horizontal red dot-dashed line in **b** indicates the threshold of self-oscillation. **c**, Maser gain spectra under various pump powers. The horizontal axis represents the detuning from the central resonator frequency $\omega_r/2\pi = 6.595\,\mathrm{GHz}$. The black dashed line represents the spectrum measured without the pump. **d**, Gain-bandwidth product versus inverted spin population. **e**, Gain versus inverted spin population, where the open symbols and dashed curves are the experimental data and theoretical curves, respectively (Methods). **f**, Maser gain spectrum versus magnetic field at a pump power of $P_{\mathrm{pump}} = -44\,\mathrm{dBm}$, yielding a gain of 23 dB.

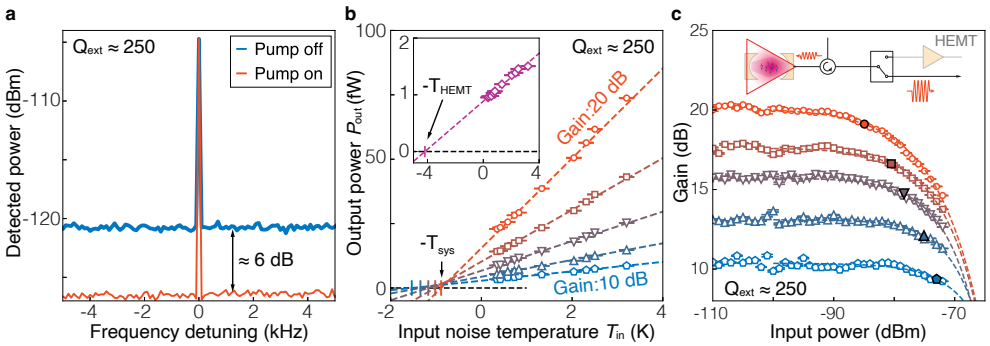


Fig. 4 Maser amplifier's noise temperature and saturation power. a, Signal-to-noise ratio (SNR) in the presence of a weak coherent probe tone with the maser amplifier turned on and off. The 'pump on' data, shown in red, is vertically shifted downwards to align the peak values for a clearer comparison of the SNRs. **b**, Noise power P_{out}, detected by a spectrum analyser, as a function of the input noise temperature T_{in} to the maser amplifier across various gains (20, 17.5, 15, 12.5, and 10 dB). Each T_{in} is corrected by taking the line attenuation and insertion losses into account (Methods). The dashed lines are linear fits, whose intersection at $P_{\mathrm{out}} = 0$ determines the system noise temperatures [24]. The inset shows the system's background noise temperature, dominated by the following HEMT amplifier, when the maser amplifier is not in operation. **c**, Gain saturation measurement showing the maser amplifier gain as a function of input signal power. The dashed curves are the fitting results, and the colored filled symbols denote the input 1 dB compression points. Inset: Schematic showing a switch to bypass the HEMT in order to prevent its saturation during these measurements.

References

[1] Yamamoto, T. *et al.* Flux-driven Josephson parametric amplifier. *Applied Physics Letters* **93**, 042510 (2008). URL https://aip.scitation.org/doi/10.1063/1.2964182.

[2] Macklin, C. *et al.* A near–quantum-limited Josephson traveling-wave parametric amplifier. *Science* **350**, 307–310 (2015). URL http://science.sciencemag.org/content/350/6258/307.

[3] Eom, B. H., Day, P. K., LeDuc, H. G. & Zmuidzinas, J. A wideband, low-noise superconducting amplifier with high dynamic range. *Nature Physics* **8**, 623–627 (2012). URL https://www.nature.com/articles/nphys2356.

[4] Malnou, M. *et al.* Three-Wave Mixing Kinetic Inductance Traveling-Wave Amplifier with Near-Quantum-Limited Noise Performance. *PRX Quantum* **2**, 010302 (2021). URL https://link.aps.org/doi/10.1103/PRXQuantum.2.010302.

[5] Clerk, A. A., Devoret, M. H., Girvin, S. M., Marquardt, F. & Schoelkopf, R. J. Introduction to quantum noise, measurement, and amplification. *Reviews of Modern Physics* **82**, 1155–1208 (2010). URL https://link.aps.org/doi/10.1103/RevModPhys.82.1155.

[6] Esposito, M., Ranadive, A., Planat, L. & Roch, N. Perspective on traveling wave microwave parametric amplifiers. *Applied Physics Letters* **119**, 120501 (2021). URL https://aip.scitation.org/doi/10.1063/5.0064892.

[7] Weber, J. Maser Noise Considerations. *Physical Review* **108**, 537–541 (1957). URL https://link.aps.org/doi/10.1103/PhysRev.108.537.

[8] Siegman, A. E. *Microwave solid-state masers* (McGraw-Hill, 1964).

[9] Shimoda, K., Takahasi, H. & H. Townes, C. Fluctuations in Amplification of Quanta with Application to Maser Amplifiers. *Journal of the Physical Society of Japan* **12**, 686–700 (1957). URL https://journals.jps.jp/doi/abs/10.1143/JPSJ.12.686.

[10] Jin, L. *et al.* Proposal for a room-temperature diamond maser. *Nature Communications* **6**, 1–8 (2015). URL https://www.nature.com/articles/ncomms9251.

[11] Day, T. *et al.* Room-Temperature Solid-State Maser Amplifier. *Physical Review X* **14**, 041066 (2024). URL https://link.aps.org/doi/10.1103/PhysRevX.14.041066. Publisher: American Physical Society.

[12] Bienfait, A. *et al.* Reaching the quantum limit of sensitivity in electron spin resonance. *Nature Nanotechnology* **11**, 253–257 (2016). URL http://www.nature.com/nnano/journal/v11/n3/full/nnano.2015.282.html.

[13] Bienfait, A. *et al.* Magnetic Resonance with Squeezed Microwaves. *Physical Review X* **7**, 041011 (2017). URL https://link.aps.org/doi/10.1103/PhysRevX.7.041011.

[14] Brubaker, B. *et al.* First Results from a Microwave Cavity Axion Search at $24\text{ }\text{ }\ensuremath{\mu}\mathrm{eV}$. *Physical Review Letters* **118**, 061302 (2017). URL https://link.aps.org/doi/10.1103/PhysRevLett.118.061302.

[15] Backes, K. M. *et al.* A quantum enhanced search for dark matter axions. *Nature* **590**, 238–242 (2021). URL https://www.nature.com/articles/s41586-021-03226-7. Number: 7845 Publisher: Nature Publishing Group.

[16] ADMX Collaboration *et al.* Search for Invisible Axion Dark Matter in the $3.3–4.2\text{ }\text{ }\ensuremath{\mu}\mathrm{eV}$ Mass Range. *Physical Review Letters* **127**, 261803 (2021). URL https://link.aps.org/doi/10.1103/PhysRevLett.127.261803. Publisher: American Physical Society.

[17] Breeze, J. D., Salvadori, E., Sathian, J., Alford, N. M. & Kay, C. W. M. Continuous-wave room-temperature diamond maser. *Nature* **555**, 493–496 (2018). URL https://www.nature.com/articles/nature25970.

[18] Sherman, A. *et al.* Diamond-based microwave quantum amplifier. *Science Advances* **8**, eade6527 (2022). URL https://www.science.org/doi/10.1126/sciadv.ade6527. Publisher: American Association for the Advancement of Science.

[19] Ng, W., Wu, H. & Oxborrow, M. Quasi-continuous cooling of a microwave mode on a benchtop using hyperpolarized NV diamond. *Applied Physics Letters* **119**, 234001 (2021). URL https://aip.scitation.org/doi/10.1063/5.0076460. Publisher: American Institute of Physics.

[20] Fahey, D. P. *et al.* Steady-State Microwave Mode Cooling with a Diamond N-V Ensemble. *Physical Review Applied* **20**, 014033 (2023). URL https://link.aps.org/doi/10.1103/PhysRevApplied.20.014033. Publisher: American Physical Society.

[21] Wu, H. *et al.* Enhanced quantum sensing with room-temperature solid-state masers. *Science Advances* **8**, eade1613 (2022). URL https://www.science.org/doi/10.1126/sciadv.ade1613. Publisher: American Association for the Advancement of Science.

[22] Ball, J. R. *et al.* Loop-gap microwave resonator for hybrid quantum systems. *Applied Physics Letters* **112**, 204102 (2018). URL https://aip.scitation.org/doi/10.1063/1.5025744.

[23] Grezes, C. *et al.* Multimode Storage and Retrieval of Microwave Fields in a Spin Ensemble. *Physical Review X* **4**, 021049 (2014). URL http://link.aps.org/doi/

10.1103/PhysRevX.4.021049.

[24] Simbierowicz, S. *et al.* Characterizing cryogenic amplifiers with a matched temperature-variable noise source. *Review of Scientific Instruments* **92**, 034708 (2021). URL https://aip.scitation.org/doi/full/10.1063/5.0028951. Tex.ids= simbierowiczCharacterizingCryogenicAmplifiers2021a publisher: American Institute of Physics.

[25] Sorokin, P. P., Lasher, G. J. & Gelles, I. L. Cross Relaxation Studies in Diamond. *Physical Review* **118**, 939–945 (1960). URL https://link.aps.org/doi/10.1103/PhysRev.118.939.

[26] Ma, C. *et al.* Four-spin cross relaxation in a hybrid quantum device. *Physical Review A* **100**, 012322 (2019). URL https://link.aps.org/doi/10.1103/PhysRevA.100.012322.

[27] Zhang, G.-Q. *et al.* Exceptional Point and Cross-Relaxation Effect in a Hybrid Quantum System. *PRX Quantum* **2**, 020307 (2021). URL https://link.aps.org/doi/10.1103/PRXQuantum.2.020307. Publisher: American Physical Society.

[28] Baier, S. *et al.* Orbital and Spin Dynamics of Single Neutrally-Charged Nitrogen-Vacancy Centers in Diamond. *Physical Review Letters* **125**, 193601 (2020). URL https://link.aps.org/doi/10.1103/PhysRevLett.125.193601. Publisher: American Physical Society.

[29] Barson, M. S. J., Krausz, E., Manson, N. B. & Doherty, M. W. The fine structure of the neutral nitrogen-vacancy center in diamond. *Nanophotonics* **8**, 1985–1991 (2019). URL https://www.degruyter.com/document/doi/10.1515/nanoph-2019-0142/html. Publisher: De Gruyter.

[30] Isoya, J., Kanda, H. & Uchida, Y. EPR studies of interstitial Ni centers in synthetic diamond crystals. *Physical Review B* **42**, 9843 (1990). URL http://journals.aps.org/prb/abstract/10.1103/PhysRevB.42.9843.

[31] Kato, K., Sasaki, R., Matsuura, K., Usami, K. & Nakamura, Y. High-cooperativity cavity magnon-polariton using a high-Q dielectric resonator. *Journal of Applied Physics* **134**, 083901 (2023). URL https://doi.org/10.1063/5.0164545.

[32] Hamamoto, T., Bhunia, A., Bhattacharya, R. K., Takahashi, H. & Kubo, Y. Dielectric microwave resonator with large optical apertures for spin-based quantum devices. *Applied Physics Letters* **124**, 234001 (2024). URL https://doi.org/10.1063/5.0208113.

[33] Faramarzi, F. *et al.* A 4–8 GHz kinetic inductance traveling-wave parametric amplifier using four-wave mixing with near quantum-limited noise performance. *APL Quantum* **1**, 036107 (2024). URL https://doi.org/10.1063/5.0208110.

[34] Parker, D. J. *et al.* Degenerate Parametric Amplification via Three-Wave Mixing Using Kinetic Inductance. *Physical Review Applied* **17**, 034064 (2022). URL https://link.aps.org/doi/10.1103/PhysRevApplied.17.034064. Publisher: American Physical Society.

[35] Probst, S., Song, F. B., Bushev, P. A., Ustinov, A. V. & Weides, M. Efficient and robust analysis of complex scattering data under noise in microwave resonators. *Review of Scientific Instruments* **86**, 024706 (2015). URL http://aip.scitation.org/doi/10.1063/1.4907935.

[36] Walls, D. & Milburn, G. J. (eds) *Quantum Optics* (Springer, Berlin, Heidelberg, 2008). URL http://link.springer.com/10.1007/978-3-540-28574-8.

[37] Kubo, Y. *et al.* Strong Coupling of a Spin Ensemble to a Superconducting Resonator. *Physical Review Letters* **105**, 140502 (2010). URL http://link.aps.org/doi/10.1103/PhysRevLett.105.140502.

[38] Choi, H. & Englund, D. Ultrastrong magnetic light-matter interaction with cavity mode engineering. *Communications Physics* **6**, 1–9 (2023). URL https://www.nature.com/articles/s42005-023-01224-x. Number: 1 Publisher: Nature Publishing Group.

[39] Collett, M. J. & Gardiner, C. W. Squeezing of intracavity and traveling-wave light fields produced in parametric amplification. *Physical Review A* **30**, 1386–1391 (1984). URL https://link.aps.org/doi/10.1103/PhysRevA.30.1386. Publisher: American Physical Society.

[40] Diniz, I. *et al.* Strongly coupling a cavity to inhomogeneous ensembles of emitters: Potential for long-lived solid-state quantum memories. *Physical Review A* **84** (2011). URL http://link.aps.org/doi/10.1103/PhysRevA.84.063810.

[41] Kurucz, Z., Wesenberg, J. H. & Mølmer, K. Spectroscopic properties of inhomogeneously broadened spin ensembles in a cavity. *Physical Review A* **83** (2011). URL http://link.aps.org/doi/10.1103/PhysRevA.83.053852.

[42] Julsgaard, B. & Mølmer, K. Dynamical evolution of an inverted spin ensemble in a cavity: Inhomogeneous broadening as a stabilizing mechanism. *Physical Review A* **86**, 063810 (2012). URL http://link.aps.org/doi/10.1103/PhysRevA.86.063810.

[43] Carmichael, H. J. *Statistical Methods in Quantum Optics 1: Master Equations and Fokker-Planck Equations* (Springer Science & Business Media, 2013). Google-Books-ID: 5hv2CAAAQBAJ.

Methods

Sample and device

Diamond sample

The diamond sample used in this work is identical to those described in previous works (Refs. [22, 23]). It was synthesized by the temperature gradient method under high-pressure and high-temperature (HPHT) conditions of 5.5 GPa and 1350 °C using an Fe-Ni-Co alloy as the metal solvent and natural diamond grains as the carbon source. A (100) plate obtained by laser-cutting and polishing was irradiated with 3 MeV electrons at a fluence of 4×10^{17} e/cm^2 at room temperature, followed by annealing at 850 °C for 2 hours in vacuum. Subsequently, it was further irradiated with 2 MeV electrons at 700 °C to a fluence of 5×10^{17} e/cm^2 and annealed at 1000 °C for 2 hours in vacuum. The final dimensions of the diamond ($3 \times 1.5 \times 0.5$ mm^3) used in this study were obtained from the central part of the plate via laser-cutting and polishing. Following electron irradiation and annealing, the concentrations of P1 centres and negatively-charged nitrogen-vacancy (NV^-) centres were measured to be approximately 16 ppm and 2 ppm, respectively.

Loop-gap resonator

The microwave resonator used in this work is a loop-gap type [22]. We determined its internal and external quality factors using the circle-fit method [35] after subtracting background amplitude oscillations to achieve a flat baseline. The results are shown in Extended Data Fig. 1 for both $Q_{\mathrm{ext}} \approx 250$ and $Q_{\mathrm{ext}} \approx 730$. The internal quality factor Q_{int} consistently stays around 3000. The resonator frequency, ω_r, is very sensitive to the distances of the two gaps. Consequently, after each disassembly and reassembly of the resonator and its enclosure to adjust Q_{ext}, ω_r varied over 6.59 GHz to 6.86 GHz upon each cooldown.

Noise temperature measurement

Y-factor method using a noise source

We characterised the noise temperature of the maser amplifier by using a procedure based on the Y-factor method with a calibrated noise source [24]. The noise source is weakly thermalised to the cold plate at about 100 mK, which allows for quasi-independent temperature control using an attached heater and thermometer. This setup enables precise control over the input noise temperature T_{in} into the maser amplifier device.

Thermal noise power is given by $P_{\mathrm{noise}} = k_{\mathrm{B}} T_{\mathrm{noise}} \delta f_{\mathrm{BW}}$, where k_{B}, T_{noise}, and δf_{BW} are the Boltzmann constant, the noise temperature, and the measurement bandwidth, respectively. When a signal with a noise temperature of T_{in} is fed into an amplifier, the output power P_{out} is given by

$$\frac{P_{\mathrm{out}}(T_{\mathrm{in}})}{G k_{\mathrm{B}} \delta f_{\mathrm{BW}}} = T_{\mathrm{in}} + T_{\mathrm{amp}}, \tag{4}$$

where G and T_{amp} are the power gain and noise temperature of the amplifier, respectively. In our experiment, without the maser amplifier, P_{out} can thus be expressed as:

$$\frac{P_{\mathrm{out}}(T_{\mathrm{in}})}{G_{\mathrm{HEMT}} k_{\mathrm{B}} \delta f_{\mathrm{BW}}} = T_{\mathrm{in}} + T_{\mathrm{HEMT}} + \frac{T_{\mathrm{bkg}}}{G_{\mathrm{HEMT}}}, \tag{5}$$

where G_{HEMT} and T_{HEMT} represent the gain and noise temperature of the HEMT amplifier, respectively. The additional noise contribution from the final room temperature amplifier, including cable attenuation from the HEMT to the room temperature setup, is denoted as T_{bkg}. Equation (5) can be approximated to Eq. (1) in the main text, considering that $G_{\mathrm{HEMT}} > 10^4$ and $T_{\mathrm{bkg}} \approx 300\,\mathrm{K}$.

Similarly, the noise power with the maser amplifier on can be expressed as:

$$\frac{P_{\mathrm{out}}(T_{\mathrm{in}})}{G_{\mathrm{maser}} G_{\mathrm{HEMT}} k_{\mathrm{B}} \delta f_{\mathrm{BW}}} = T_{\mathrm{in}} + T_{\mathrm{maser}} + \frac{T_{\mathrm{HEMT}}}{G_{\mathrm{maser}}} + \frac{T_{\mathrm{bkg}}}{G_{\mathrm{maser}} G_{\mathrm{HEMT}}}, \tag{6}$$

where G_{maser} and T_{maser} represent the gain and noise temperature of the maser amplifier, respectively. Therefore, Eq. (6) can be approximated to Eq. (2) in the main text under the same considerations.

Impact of insertion losses and attenuation on noise temperature

In our setup, a directional coupler and a circulator, as well as lossy non-superconducting cables, are placed between the noise source and the maser amplifier. Their insertion losses and attenuations must, therefore, be taken into account in the evaluation of the input noise temperature T_{in}, as they attenuate the noise photons from the noise source. To model this effect, we employ the beam-splitter model [36]. If the j-th component in the transmission line has an insertion loss β_j, the number of noise photons n_{j+1} can be expressed as

$$n_{j+1} = \beta_j \left(n_j + \frac{1}{2} \right) + (1 - \beta_j) \left(n_{\mathrm{th}} + \frac{1}{2} \right), \tag{7}$$

where n_j is the number of input noise photons of the j-th component, and n_{th} is the thermal noise photons corresponding to the physical temperature of the component. All the presented values of T_{in} are corrected using Eq. (7) based on the measurements detailed in the following.

Noise temperature of baseline

We measured the noise temperature at several frequencies around the maser peak gain, both with the pump on and off, as shown in Extended Data Fig. 2. First, we measured the noise temperature with the pump off, namely, T_{HEMT}. To minimize the absorption effect by the spins, which is equivalent to having additional attenuation along the line, the magnetic field was detuned from the resonance of $\mathrm{P1}_+$.

Under these conditions, as seen in Extended Data Fig. 2, the noise temperatures are measured to be between 2 and 4 K, in reasonable agreement with the values reported in the HEMT's datasheet. The oscillations are mostly attributed to small impedance mismatches among the components along the measurement chain from 10 mK up to the HEMT amplifier. At the resonance frequency $\omega_r \approx 6.6$ GHz, it reaches ≈ 4.2 K, which is used as the HEMT's noise temperature T_{HEMT} in the main text. During this measurement with the pump off, we disconnected both the pump and cancellation lines and terminated at room temperature to minimize the noise from the room-temperature setup, especially from the amplifier in the cancellation line (see Supplementary Information).

When the pump and cancellation tones are turned on and tuned for maser amplifier's gain of 20 dB, the noise baseline increases by approximately 1 K over the entire frequency range (except near ω_r, i.e., the maser amplifier frequency), most likely due to noise coming from the room-temperature amplifier connected to the "Cancellation" line. The significant increase of the noise around ~ -100 MHz is due to the pump.

Detailed line attenuation characterization

In order to accurately estimate the power of the pump and probe tones arriving at the input of the maser amplifier device, we independently characterised the attenuation of both the probe and pump lines in a separate cooldown. To this end, we measured the transmission coefficients over the "symmetric lines", i.e, pairs of lines with identical configurations, including coaxial cable materials, lengths, and attenuators at each temperature stage, as illustrated in Extended Data Fig. 3. These symmetric lines were interconnected by a short, low-loss coaxial cable at the mixing chamber stage.

We also characterised the attenuation of the cables and components in the Probe line at the mixing chamber stage, specifically from the infrared filter through the circulator, noise source, directional coupler, and the final circulator to the input of the maser device (see also Supplementary Information). This was performed using two mechanical microwave switches (Radiall, R573423600), as depicted in Extended Data Fig. 3. Four measurement paths (Ch. 1–Ch. 4) were established for this purpose. Channels 1 and 2 correspond to the paths from the noise source to the maser amplifier device and from the infrared filter to the noise source, respectively. Channel 3 was used to isolate the attenuation introduced by the components measured in Ch. 1 and Ch. 2 by using a low-loss flexible coaxial cable. Channel 4 was used to estimate the attenuation of the low-loss flexible coaxial cables used to connect the components by comparing with Ch. 3. The results of these measurements are summarized in Table 1. Note that the insertion loss of the mechanical switches must also be taken into account in the calculation of Eq. (7) for the noise temperature measurement; here we relied on the value on the datasheet of 0.3 dB.

Extracting spin information through resonator

Single Spin Coupling Constant

The single-spin coupling constant g_0, which represents the interaction strength between a single P1 centre and a single microwave photon in a resonator, is expressed

as [37]

$$g_0 = -\gamma_e \delta B_0 \langle -1/2|\mathbf{S}|+1/2\rangle, \tag{8}$$

where γ_e and δB_0 denotes the gyromagnetic ratio of the electron spin and the magnetic vacuum fluctuation of the resonator, respectively, and $\mathbf{S}$ is the spin vector operator with $|-1/2\rangle$ and $|+1/2\rangle$ are the P1 centre's electron spin eigenstates. The magnetic vacuum fluctuation is given by

$$\delta B_0 = \sqrt{\frac{\mu_0 \hbar \omega_r}{2\mathcal{V}_{\text{eff}}}}, \tag{9}$$

where μ_0, ω_r, and $\mathcal{V}_{\text{eff}}$ are the vacuum permeability, the resonator frequency, and the effective mode volume of the resonator, respectively. $\mathcal{V}_{\text{eff}}$ is defined as the ratio of the integral of the magnetic field energy density over the whole resonator mode volume V to the maximum magnetic energy density [38]

$$\mathcal{V}_{\text{eff}} = \frac{\int_V |\mathbf{B}(\mathbf{r})|^2/\mu(\mathbf{r}) \mathrm{d}V}{|\mathbf{B}(\mathbf{r}_0)|^2/\mu(\mathbf{r}_0)}, \tag{10}$$

where $\mathbf{B}(\mathbf{r})$ is the magnetic field in the resonator, maximized at the position $\mathbf{r}_0$. Using a finite element simulation software, COMSOL Multiphysics, the effective resonator mode volume $\mathcal{V}_{\text{eff}}$ of our loop-gap resonator is estimated to be approximately $\mathcal{V}_{\text{eff}} \approx 2.5 \times 10^{-8}\,\mathrm{m}^3$. Therefore, the single-spin coupling constant of the P1 centre with $S = 1/2$ is obtained to be $g_0 \approx 2\pi \times 0.15\,\mathrm{Hz}$.

Input-output theory

To determine the number of inverted or non-inverted spins through the resonator reflection $r(\omega)$, we employed the input-output theory [39] for a coupled resonator-spin ensemble system with a coherent probe tone $\alpha_{\text{in}} = \alpha_0 e^{-i\omega t}$ [11, 23]. The Hamiltonian can be expressed using the Tavis-Cummings model with Holstein-Primakoff approximation [40–42] as follows:

$$H/\hbar = \omega_r a^\dagger a + \frac{1}{2}\sum_{j=1}^{N} \omega_j s_j^\dagger s_j + \sum_{j=1}^{N} g_j \left(s_j^\dagger a + s_j a^\dagger\right) - i\sqrt{\kappa_{\text{ext}}}(\alpha_{\text{in}} a^\dagger - \alpha_{\text{in}}^* a), \tag{11}$$

where a (s_j) and $a^\dagger$ ($s_j^\dagger$) denote the annihilation and creation operators for the resonator mode (j-th spin), respectively. In addition, N represents the number of spins, and g_j is the single spin coupling constant between the resonator and the j-th spin. $\kappa_{\text{ext}} = \omega_r/Q_{\text{ext}}$ and $\kappa_{\text{int}} = \omega_r/Q_{\text{int}}$ are the external and internal loss rates of the resonator, with Q_{ext} (Q_{int}) representing the external (internal) quality factor.

The spin function $K(\omega)$

Following the standard method for deriving the reflection coefficient [39], we obtain

$$r(\omega) = \frac{i\kappa_{\mathrm{ext}}}{(\omega - \omega_r) + i\frac{\kappa_{\mathrm{ext}}+\kappa_{\mathrm{int}}}{2} \pm K(\omega)} - 1, \tag{12}$$

where $K(\omega)$, called the "spin function", includes all information about the spin ensemble. As will be discussed in the following section, $K(\omega)$ is linked to the spin susceptibility [23] and is defined as shown in Refs. [40–42],

$$K(\omega) = \sum_{j=1}^{N} \frac{g_j^2}{(\omega - \omega_j) + i\gamma_j/2} = \frac{g_{\mathrm{ens}}^2}{(\omega - \omega_s) + i\Gamma/2}, \tag{13}$$

with $g_{\mathrm{ens}} = \sum_j g_j = g_0\sqrt{N}$ representing the ensemble coupling constant between the resonator and the spin ensemble. The decay rate of individual spins is denoted by γ_j, while ω_s and $\Gamma/2$ represent the centre frequency and the half-width at half-maximum (HWHM) of the spin ensemble, respectively, assumed to follow a Lorentzian distribution here. The sign in front of $K(\omega)$ in Eq. (12) represents the state of the spin ensemble, i.e., a positive sign $(+)$ corresponds to an inverted spin ensemble, whereas a negative sign $(-)$ represents a non-inverted spin ensemble.

We modify $K(\omega)$ to incorporate the spin polarization $\bar{\rho} = \Delta N/N_{\mathrm{tot}}$, where $\Delta N = N_l - N_u$ represents the population difference between the lower and upper levels of the $\mathrm{P1}_+$ state, and $N_{\mathrm{tot}} = N_l + N_u$ is the total number of spins in the $\mathrm{P1}_+$ transition. In a system with a population difference ΔN, the ensemble coupling constant g_{ens} is replaced by the effective coupling constant $g_{\mathrm{ens,eff}}$, defined as $g_{\mathrm{ens,eff}}^2 = g_0^2\Delta N$. Consequently, $K(\omega)$ is reformulated in terms of $\bar{\rho}$ as

$$K(\omega) = \frac{g_{\mathrm{ens,eff}}^2}{(\omega - \omega_s) + i\Gamma/2} = \frac{g_0^2\Delta N}{(\omega - \omega_s) + i\Gamma/2} = \frac{\bar{\rho}g_{\mathrm{ens,total}}^2}{(\omega - \omega_s) + i\Gamma/2}, \tag{14}$$

where $g_{\mathrm{ens,total}}^2 = g_0^2 N_{\mathrm{total}}$ represents the "conventional" collective coupling constant, assuming all spins are polarized into the lower energy state. The sign of $K(\omega)$ reflects the sign of ΔN; it becomes negative in the case of population inversion and positive in a non-inverted state. To ensure consistency with Eq. (12), we rewrite the reflection coefficient $r(\omega)$ as follows

$$r(\omega) = \frac{i\kappa_{\mathrm{ext}}}{(\omega - \omega_r) + i\frac{\kappa_{\mathrm{ext}}+\kappa_{\mathrm{int}}}{2} - K(\omega)} - 1. \tag{15}$$

Measurement of population differences ΔN

The function $K(\omega)$ can be expressed in terms of the reflection coefficient $r(\omega)$ by rearranging Eq. (15):

$$K(\omega) = (\omega - \omega_r) + \frac{i}{2}\left(\kappa_{\mathrm{int}} + \kappa_{\mathrm{ext}}\frac{r(\omega)-1}{r(\omega)+1}\right), \tag{16}$$

which allows $K(\omega)$ to be directly determined from the experimentally obtained $r(\omega)$ data. Extended Data Fig. 4 shows such examples converted from experimentally obtained data and fits using the imaginary parts of Eq. (14).

In an ideal spin ensemble, the imaginary part of $K(\omega)$ exhibits a Lorentzian profile, enabling straightforward determination of the population difference ΔN by fitting the measured spectrum using the function:

$$y = y_0 + \frac{A}{(x-x_0)^2 + B^2}. \tag{17}$$

From this function and the imaginary part of Eq. (14), the population difference ΔN can be extracted as $\Delta N = A/g_0^2 B$.

However, significant deviations from the ideal Lorentzian profile are observed under certain experimental conditions. Immediately after initiating the pump, and before reaching the steady state, the spectrum becomes distorted due to the rapid inversion of the spins near the centre of the distribution, while those farther from the centre remain non-inverted. Furthermore, even in the steady state, intermediate pump powers lead to partial inversion of the spin ensemble, resulting in non-uniform inversion and persistent spectral distortion. This behavior is illustrated in Extended Data Fig. 4. Panel a shows spectra at selected time points extracted from the time evolution in Fig. 3a of the main text. Among these, the spectra at 146.6 and 326.7 seconds clearly exhibit transient distortions following pump initiation. Panel b shows spectra at various pump powers extracted from the gain profiles in Fig. 3b. Notably, the spectrum at a pump power of -59 dBm exhibits pronounced steady-state distortion due to partial inversion.

To accurately account for these spectral conditions, we employ a two-Lorentzian fitting model in which the spectrum is represented as a superposition of two separate Lorentzian contributions; one representing the inverted upper-level spins and the other the lower-level spins:

$$y = y_0 + \frac{A_1}{(x-x_1)^2 + B_1^2} - \frac{A_2}{(x-x_2)^2 + B_2^2}. \tag{18}$$

The results of fits using this model are illustrated in Extended Data Fig. 4. From this fitting model, the population difference ΔN can be described as

$$\Delta N = \frac{1}{g_0^2}\left(\frac{A_2}{B_2} - \frac{A_1}{B_1}\right). \tag{19}$$

Maser gain

The peak maser gain is defined by the absolute square of the reflection coefficient $r(\omega)$ at the resonance, where $\omega = \omega_r = \omega_s$. According to Eq. (15), this relationship can be expressed as

$$G = |r(\omega)|^2 = \frac{(\kappa_{\text{ext}} - \kappa_{\text{int}} + |\kappa_{\text{s}}|)^2}{(\kappa_{\text{ext}} + \kappa_{\text{int}} - |\kappa_{\text{s}}|)^2}, \tag{20}$$

where we defined a new parameter, $\kappa_s = 4g_{\text{ens}}^2/\Gamma = \text{Im}[2K(\omega_r = \omega_s)]$ [11, 42], as the "spin transition rate". This parameter quantifies the effective transition rate of the spin ensemble to the resonator mode, i.e., the rate at which spins undergo upwards (downwards) transitions per unit time through the stimulated emission (absorption) with a rate $\Gamma_{\text{s}} = 4g_0^2/\Gamma$. Moreover, κ_{s} is directly correlated with the "magnetic quality factor" Q_{mag} [8, 18], which characterises a spin ensemble system as a maser gain medium:

$$Q_{\text{mag}} = \frac{1}{\eta\chi''} = \frac{1}{\eta \cdot \text{Im}[2K(\omega_r = \omega_s)/(\omega_r\eta)]} = \frac{\omega_r\Gamma}{4g_{\text{ens}}^2} = \frac{\omega_r}{\kappa_s}, \tag{21}$$

where η is the magnetic field filling factor and χ'' is the imaginary part of the spin susceptibility at resonance, defined as $\chi(\omega) = -2K(\omega)/(\omega_r\eta)$ [23].

Using Eq. (20), we calculated the gains $G(\omega_r = \omega_s)$ for the two external quality factors, $Q_{\text{ext}} \approx 250$ and 730, used in the experiments. The results are shown as dashed curves in Fig. 3e.

Modeling spin dynamics

Semi-classical Rate Equations

We modeled the dynamics of our diamond maser amplifier system as detailed below and solved them using semi-classical rate equations [25]. Although quantum Langevin equations would yield equivalent results [10, 11], our lack of expertise with that numerical treatment led us to opt for a semi-classical approach. The system under consideration, as depicted in Extended Data Fig. 5a, consists of eight energy levels, which include two levels of the "fast-relaxing spins" and the three two-level systems associated with the P1 centres nuclear spin states, P1_+, P1_0, and P1_-. This configuration leads to eight rate equations, in addition to a photon number rate equation, to describe the population dynamics and photon numbers within the system. However, due to the computational complexity of solving nine equations, we simplified the model to seven equations by combining the two levels of P1_- with the fast-relaxing spins. The resulting set of seven rate equations, including the photon number rate equation, are represented as follows [25, 43]:

$$\dot{N}_1 = \Gamma_{41}N_4 + \frac{\Gamma_{\text{cr}}}{N_{\text{tot}}^3}(N_2^2N_4N_6 - N_5^2N_1N_3) - \Gamma_s n(N_1 - N_4), \tag{22}$$

$$
\begin{aligned}
\dot{N}_2 &= \Gamma_{52} N_5 - 2\frac{\Gamma_{\mathrm{cr}}}{N_{\mathrm{tot}}^3}(N_2^2 N_4 N_6 - N_5^2 N_1 N_3) - \Gamma_{\mathrm{p}}(N_2 - N_5),\\
\dot{N}_3 &= \Gamma_{63}^{\mathrm{eff}} N_6 + \frac{\Gamma_{\mathrm{cr}}}{N_{\mathrm{tot}}^3}(N_2^2 N_4 N_6 - N_5^2 N_1 N_3),\\
\dot{N}_4 &= -\Gamma_{41} N_4 - \frac{\Gamma_{\mathrm{cr}}}{N_{\mathrm{tot}}^3}(N_2^2 N_4 N_6 - N_5^2 N_1 N_3) + \Gamma_s n(N_1 - N_4),\\
\dot{N}_5 &= -\Gamma_{52} N_5 + 2\frac{\Gamma_{\mathrm{cr}}}{N_{\mathrm{tot}}^3}(N_2^2 N_4 N_6 - N_5^2 N_1 N_3) + \Gamma_{\mathrm{p}}(N_2 - N_5),\\
\dot{N}_6 &= -\Gamma_{63}^{\mathrm{eff}} N_6 - \frac{\Gamma_{\mathrm{cr}}}{N_{\mathrm{tot}}^3}(N_2^2 N_4 N_6 - N_5^2 N_1 N_3),
\end{aligned}
$$

where N_i represents the number of spins of each level, Γ_{41}, Γ_{52}, and Γ_{63} are the relaxation rates of each transition, Γ_{cr} is the four-spin cross-relaxation rate, and $\Gamma_s = 4g_0^2/\Gamma$ is the stimulated emission rate. The rate equation for the intra-resonator photon number n is:

$$
\dot{n} = -\kappa_{\mathrm{tot}} n - \Gamma_s n(N_1 - N_4) + \Gamma_s N_4. \tag{23}
$$

Cross-relaxation rate

The cross-relaxation rate Γ_{cr} in our system cannot be directly measured due to the presence of the "fast-relaxing spins", contrasting with the previous reports [25–27]. To estimate this rate indirectly, we compared computational results from the rate equations with experimental results obtained under various pump powers, as depicted in Extended Data Fig. 5b and explained in the next subsection. We determined Γ_{cr} to be within the range of ~ 1 to 10 mHz, with the parameters listed in Tables 2 and 3. While previously reported cross-relaxation rates for highly nitrogen-doped diamonds typically range from ~ 10 Hz to ~ 100 Hz [25, 26], theoretical models of the four-spin interactions imply that $\Gamma_{\mathrm{cr}} \propto d^6$ [26], where d denotes the spin density. This supports our findings of $\Gamma_{\mathrm{cr}} \sim$ mHz, as the P1 centre density in our diamond sample of ≈ 16 ppm is considerably lower than the > 100 ppm in those previous studies.

Calculation of pump rate Γ_{p}

Spins absorb incoming microwave pump tones and are excited to the upper state, a process governed by the same underlying physics as stimulated emission. Therefore, the photon absorption rate, i.e., the pump rate Γ_{p}, is calculated as a product of the stimulated emission rate and the number of incoming photons, as described in Eqs. (7.7) and (7.8) on p.260 in Ref. [43]:

$$
\Gamma_{\mathrm{p}} = \frac{g_0^2 \Gamma}{(\omega_p - \omega_s)^2 + \Gamma^2/4} n_{\mathrm{in}}, \tag{24}
$$

where ω_p is the pump frequency, ω_s is the average spin resonance frequency of $\mathrm{P1}_0$, and n_{in} is the number of input photons. The expression $g_0^2\Gamma/\left[(\omega_p - \omega_s)^2 + \Gamma^2/4\right]$ on

the right-hand side is the rigorous stimulated emission rate with detuning between ω_p and ω_s.

From the input-output theory, n_{in} with a coherent pump tone $\beta_{\mathrm{in}} = \beta_0 e^{-i\omega t}$ applied to a single-port resonator is expressed as

$$n_{\mathrm{in}} = \frac{4\kappa_{\mathrm{ext}}}{\kappa_{\mathrm{tot}}^2 + 4(\omega_p - \omega_r)^2}|\beta_0|^2 = \frac{4\kappa_{\mathrm{ext}}}{\kappa_{\mathrm{tot}}^2 + 4(\omega_p - \omega_r)^2}\frac{P_{\mathrm{in}}}{\hbar\omega}, \tag{25}$$

where $P_{\mathrm{in}} = \hbar\omega|\beta_0|^2$ denotes the input pump power, and $\kappa_{\mathrm{tot}} = \kappa_{\mathrm{ext}} + \kappa_{\mathrm{int}}$ is the total loss rate of the resonator. Therefore, the pump rate Γ_{p} can be expressed as a function of P_{in} as follows;

$$\Gamma_{\mathrm{p}}(P_{\mathrm{in}}) = \frac{g_0^2\Gamma}{(\omega_p - \omega_s)^2 + \Gamma^2/4} \cdot \frac{4\kappa_{\mathrm{ext}}}{\kappa_{\mathrm{tot}}^2 + 4(\omega_p - \omega_r)^2}\frac{P_{\mathrm{in}}}{\hbar\omega_p}. \tag{26}$$

During maser operation, the pump frequency ω_p is tuned to match the resonance frequency of the $\mathrm{P1}_0$ spins, i.e., $\omega_p = \omega_s = \omega_0$, but it is off-resonance with the resonator, thus $\omega_p \neq \omega_r$. Figure 5b displays the population difference in the P1+ transition, $\Delta N_{\mathrm{P1+}}$, plotted against the calculated pump rates Γ_{p}. This population difference is extracted using the spin function $K(\omega)$, as discussed in the above section. The plot also includes overlayed simulation results from the rate equations Eqs. (22) and (23).

Self-oscillation threshold

If the photons produced by stimulated emission exceed the resonator losses, the system enters the self-oscillating or free-running maser regime. In this regime, the maser is capable of emitting microwave photons into the resonator without the need for an externally applied probe tone. The threshold population difference ΔN_{thr} can be calculated from the photon number rate equation given in Eq. (23) [43]. At the threshold, the two terms in the equation are balanced, hence,

$$0 = -\kappa_{\mathrm{tot}} n_{\mathrm{ss}} - \Gamma_s n_{\mathrm{ss}} \Delta N_{\mathrm{thr}} + \Gamma_s N_4^{\mathrm{thr}}, \tag{27}$$

where N_4^{thr} is the number of spins in the state 4 at the threshold and n_{ss} is the photon number in the steady state in the free-running maser regime. Rearranging this equation gives

$$\Delta N_{\mathrm{thr}} = -\frac{\kappa_{\mathrm{tot}}}{\Gamma_s} + \frac{N_4^{\mathrm{thr}}}{n_{\mathrm{ss}}}. \tag{28}$$

The second term can often be neglected since typically $n_{\mathrm{ss}} \gg 1$. Therefore,

$$|\Delta N_{\mathrm{thr}}| \approx \frac{\kappa_{\mathrm{tot}}}{\Gamma_s} = \frac{\kappa_{\mathrm{tot}}\Gamma}{4g_0^2}. \tag{29}$$

In the case of $Q_{\mathrm{ext}} \approx 250$, $|\Delta N_{\mathrm{thr}}|$ is approximately 4.81×10^{14}, while for $Q_{\mathrm{ext}} \approx 730$, it is approximately 2.42×10^{14}. These thresholds are shown as the red dot-dashed lines in Fig. 3b and d in the main text.

Data availability

The data presented in the figures with analysis codes are available from the authors upon reasonable request.

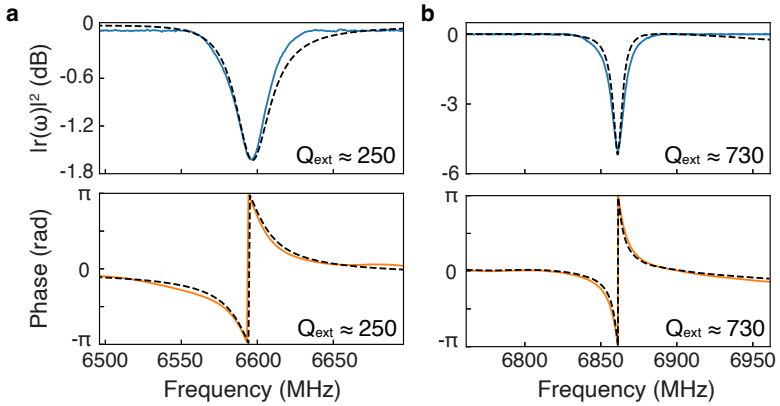
Acknowledgements. We thank J. Pla, Ç.O. Girit, P. Bertet, A. Bienfait, D. Xiao, R.-B. Liu, J.J.L. Morton, K. Mølmer, E. Flurin, M. Hatifi, F. Quijandría, J. Teufel, Y. Ota, S. Iwamoto, and S. Kono for their discussions, and M. Ishida for assistance with device illustration. We are also grateful to the members of the Hybrid Quantum Device Team within the Science and Technology Group and the Experimental Quantum Information Physics Unit at Okinawa Institute of Science and Technology (OIST) Graduate University for their insights. Additionally, we acknowledge the support from S. Ikemiyagi, M. Kuroda, and P. Kennedy at the Engineering Section of OIST. This work was supported by the Proof-of-Concept (PoC) program by OIST Innovation, the JST Moonshot R&D Program (Grant No. JPMJMS2066), JST-PRESTO (Grant No. JPMJPR15P7), JSPS KAKENHI Grant-in-Aid for Scientific Research (B) (Grant No. 18H01817), Grant-in-Aid for Scientific Research on Innovative Areas (Grant No. 18H04295), the Science Research Promotion Fund from the Promotion and Mutual Aid Corporation for Private Schools of Japan (PMAC), and the Research Encouragement Grant from the AGC Inc. Research Foundation. M.O. and T.H. acknowledge financial support from the JSPS Grant-in-Aid for Fellows (Grant Nos. 23KJ2135 and 24KJ2178), and J.R.B. acknowledges support from OIST Graduate University.

Author contributions. M.O. and C.-P.L. contributed equally to this work and were primarily responsible for data collection with partial assistance from V.P.M.S., T.H., I.K., and Y.Ku. M.O. and C.-P.L. analysed the data with assistance from T.H., I.K., V.P.M.S., and Y.Ku. Y.Ku. conceived the project and initiated the preliminary experiments with J.R.B. and P.M. S.O., T.O., Y.Ko., and J.I. were responsible for the preparation of the diamond sample. Y.Ku. and H.T. jointly supervised the project. All authors contributed to the manuscript.

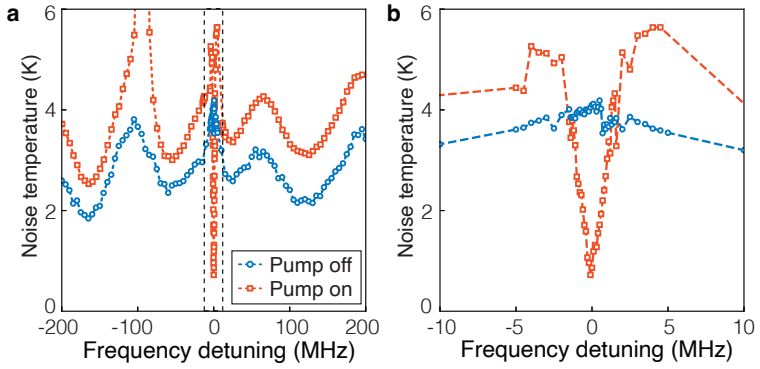
Competing interests. The authors declare no competing interests.

Supplementary information. Supplementary information is also available.

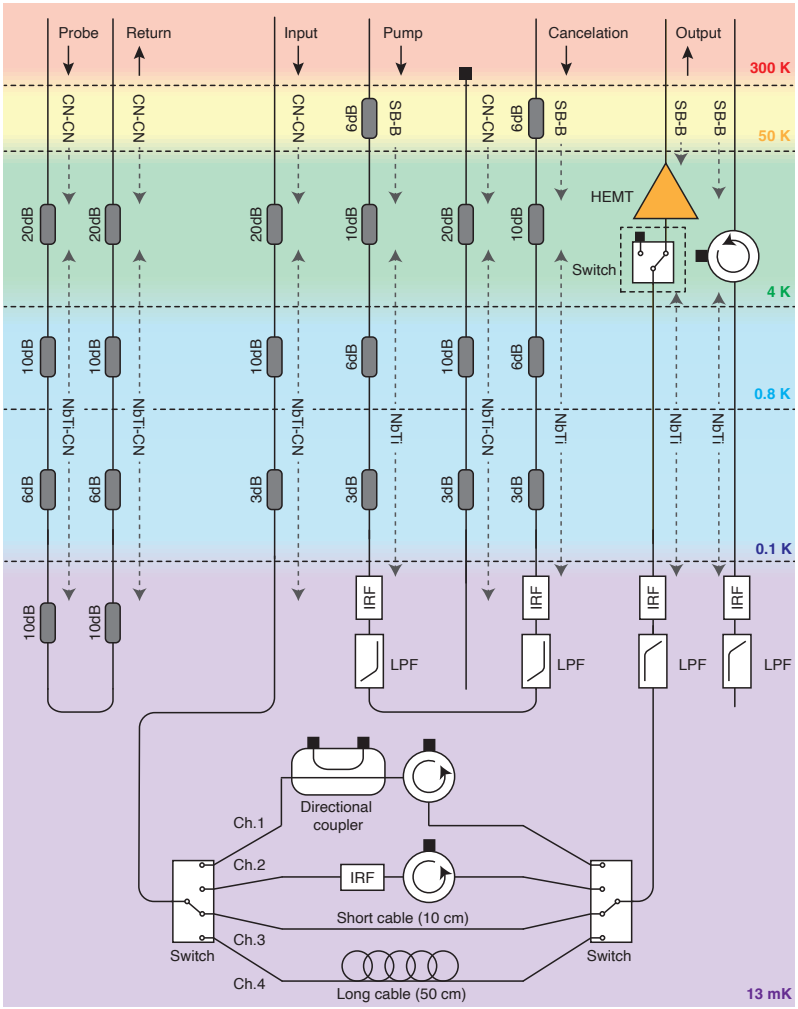
Extended Data



Extended Data Fig. 1 Quality factors of the bare resonator. Magnitude (upper panels) and phase (lower panels) of the resonator reflection coefficient $r(\omega)$ for (**a**) $Q_{\rm ext} \approx 250$ and (**b**) $Q_{\rm ext} \approx 730$. The black dashed lines represent the fits.



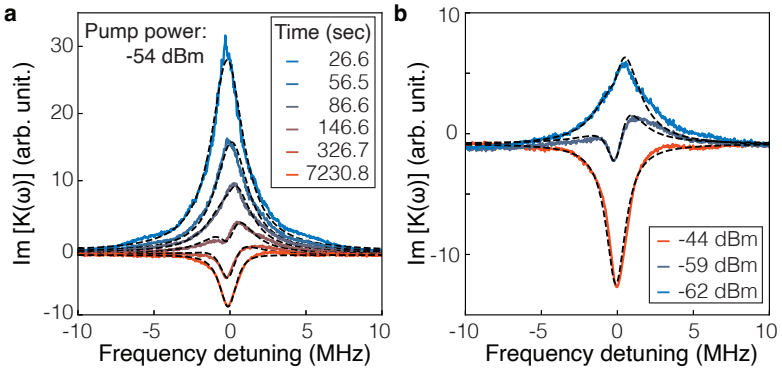
Extended Data Fig. 2 Noise temperature measurements over wide frequency range. Noise temperature as a function of frequency detuning, measured with the pump on (red squares), and with the pump off and an off-resonant magnetic field for $P1_+$ (blue circles). **a**, Wide range: ± 200 MHz. **b**, Zoomed-in view: ± 10 MHz, corresponding to the dashed window in (**a**).



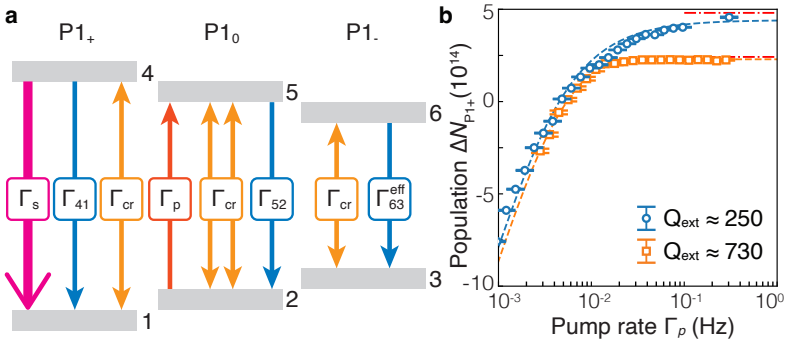
Extended Data Fig. 3 Cryogenic wiring used to characterise the line attenuations. The vertical arrows next to each line denote the materials used for the inner and outer conductors, with CN, B, and SB representing cupronickel, beryllium copper, and silver-plated beryllium copper, respectively.

Extended Data Table 1 Line attenuations

Line	Attenuation value (dB)
Probe	53.3
Pump, Cancellation	27.6
Channel 1	1.26
Channel 2	1.50



Extended Data Fig. 4 Measured spin function $K(\omega)$. Imaginary parts of $K(\omega)$ obtained from the measured maser gain spectra, with fits (black dashed lines) with Eq. (18). The data shown in **a** correspond to selected time points from the time dynamics presented in Fig. 3a in the main text at a pump power of -54 dBm, while those in **b** represent gain spectra under the three pump powers after the gain was stabilized.



Extended Data Fig. 5 Rate equation model and comparison to measurements. a, Energy level diagram of P1 centre and the relaxation rates used in the rate-equation model. **b**, Steady-state population difference ΔN_{P1_+} between the lower and upper $\mathrm{P1}_+$ states, obtained from measured $r(\omega)$ using Eq. (16) in the Materials and Methods, plotted versus the pump rate Γ_p calculated from Eq. (26) based on the applied pump power P_in. The dashed lines indicate the results of rate-equation simulations, and the red dot-dashed lines represent the threshold of both Q_ext values.

Extended Data Table 2 Relaxation rates used in the rate-equation simulation. The values of Γ_{41} and Γ_{63} are determined from T_1 measurements of the $\mathrm{P1}_+$ and $\mathrm{P1}_-$ transitions shown in Fig. 2f.

Parameter	$\Gamma_{41}/2\pi$ (Hz)	$\Gamma_{52}/2\pi$ (Hz)	$\Gamma_{63}/2\pi$ (Hz)	$\Gamma_{\mathrm{cr}}/2\pi$ (Hz)
Value	9.6×10^{-5}	9.6×10^{-5}	1.5×10^{-4}	6.0×10^{-2}

Extended Data Table 3 Resonator and spin parameters used in the rate-equation simulations.

Q_{ext}	$\omega_r/2\pi$ (Hz)	$\kappa_{\mathrm{ext}}/2\pi$ (Hz)	$\kappa_{\mathrm{int}}/2\pi$ (Hz)	$\Gamma/2/2\pi$ (Hz)
250	6.59×10^9	25×10^6	2.6×10^6	0.75×10^6
730	6.86×10^9	9.4×10^6	2.2×10^6	0.90×10^6

References

[1] Yamamoto, T. *et al.* Flux-driven Josephson parametric amplifier. *Applied Physics Letters* **93**, 042510 (2008). URL https://aip.scitation.org/doi/10.1063/1.2964182.

[2] Macklin, C. *et al.* A near–quantum-limited Josephson traveling-wave parametric amplifier. *Science* **350**, 307–310 (2015). URL http://science.sciencemag.org/content/350/6258/307.

[3] Eom, B. H., Day, P. K., LeDuc, H. G. & Zmuidzinas, J. A wideband, low-noise superconducting amplifier with high dynamic range. *Nature Physics* **8**, 623–627 (2012). URL https://www.nature.com/articles/nphys2356.

[4] Malnou, M. *et al.* Three-Wave Mixing Kinetic Inductance Traveling-Wave Amplifier with Near-Quantum-Limited Noise Performance. *PRX Quantum* **2**, 010302 (2021). URL https://link.aps.org/doi/10.1103/PRXQuantum.2.010302.

[5] Clerk, A. A., Devoret, M. H., Girvin, S. M., Marquardt, F. & Schoelkopf, R. J. Introduction to quantum noise, measurement, and amplification. *Reviews of Modern Physics* **82**, 1155–1208 (2010). URL https://link.aps.org/doi/10.1103/RevModPhys.82.1155.

[6] Esposito, M., Ranadive, A., Planat, L. & Roch, N. Perspective on traveling wave microwave parametric amplifiers. *Applied Physics Letters* **119**, 120501 (2021). URL https://aip.scitation.org/doi/10.1063/5.0064892.

[7] Weber, J. Maser Noise Considerations. *Physical Review* **108**, 537–541 (1957). URL https://link.aps.org/doi/10.1103/PhysRev.108.537.

[8] Siegman, A. E. *Microwave solid-state masers* (McGraw-Hill, 1964).

[9] Shimoda, K., Takahasi, H. & H. Townes, C. Fluctuations in Amplification of Quanta with Application to Maser Amplifiers. *Journal of the Physical Society of Japan* **12**, 686–700 (1957). URL https://journals.jps.jp/doi/abs/10.1143/JPSJ.12.686.

[10] Jin, L. *et al.* Proposal for a room-temperature diamond maser. *Nature Communications* **6**, 1–8 (2015). URL https://www.nature.com/articles/ncomms9251.

[11] Day, T. *et al.* Room-Temperature Solid-State Maser Amplifier. *Physical Review X* **14**, 041066 (2024). URL https://link.aps.org/doi/10.1103/PhysRevX.14.041066. Publisher: American Physical Society.

[12] Bienfait, A. *et al.* Reaching the quantum limit of sensitivity in electron spin resonance. *Nature Nanotechnology* **11**, 253–257 (2016). URL http://www.nature.com/nnano/journal/v11/n3/full/nnano.2015.282.html.

[13] Bienfait, A. *et al.* Magnetic Resonance with Squeezed Microwaves. *Physical Review X* **7**, 041011 (2017). URL https://link.aps.org/doi/10.1103/PhysRevX.7.041011.

[14] Brubaker, B. *et al.* First Results from a Microwave Cavity Axion Search at $24\text{ }\text{ }\ensuremath{\mu}\mathrm{eV}$. *Physical Review Letters* **118**, 061302 (2017). URL https://link.aps.org/doi/10.1103/PhysRevLett.118.061302.

[15] Backes, K. M. *et al.* A quantum enhanced search for dark matter axions. *Nature* **590**, 238–242 (2021). URL https://www.nature.com/articles/s41586-021-03226-7. Number: 7845 Publisher: Nature Publishing Group.

[16] ADMX Collaboration *et al.* Search for Invisible Axion Dark Matter in the $3.3–4.2\text{ }\text{ }\ensuremath{\mu}\mathrm{eV}$ Mass Range. *Physical Review Letters* **127**, 261803 (2021). URL https://link.aps.org/doi/10.1103/PhysRevLett.127.261803. Publisher: American Physical Society.

[17] Breeze, J. D., Salvadori, E., Sathian, J., Alford, N. M. & Kay, C. W. M. Continuous-wave room-temperature diamond maser. *Nature* **555**, 493–496 (2018). URL https://www.nature.com/articles/nature25970.

[18] Sherman, A. *et al.* Diamond-based microwave quantum amplifier. *Science Advances* **8**, eade6527 (2022). URL https://www.science.org/doi/10.1126/sciadv.ade6527. Publisher: American Association for the Advancement of Science.

[19] Ng, W., Wu, H. & Oxborrow, M. Quasi-continuous cooling of a microwave mode on a benchtop using hyperpolarized NV diamond. *Applied Physics Letters* **119**, 234001 (2021). URL https://aip.scitation.org/doi/10.1063/5.0076460. Publisher: American Institute of Physics.

[20] Fahey, D. P. *et al.* Steady-State Microwave Mode Cooling with a Diamond N-V Ensemble. *Physical Review Applied* **20**, 014033 (2023). URL https://link.aps.org/doi/10.1103/PhysRevApplied.20.014033. Publisher: American Physical Society.

[21] Wu, H. *et al.* Enhanced quantum sensing with room-temperature solid-state masers. *Science Advances* **8**, eade1613 (2022). URL https://www.science.org/doi/10.1126/sciadv.ade1613. Publisher: American Association for the Advancement of Science.

[22] Ball, J. R. *et al.* Loop-gap microwave resonator for hybrid quantum systems. *Applied Physics Letters* **112**, 204102 (2018). URL https://aip.scitation.org/doi/10.1063/1.5025744.

[23] Grezes, C. *et al.* Multimode Storage and Retrieval of Microwave Fields in a Spin Ensemble. *Physical Review X* **4**, 021049 (2014). URL http://link.aps.org/doi/

10.1103/PhysRevX.4.021049.

[24] Simbierowicz, S. *et al.* Characterizing cryogenic amplifiers with a matched temperature-variable noise source. *Review of Scientific Instruments* **92**, 034708 (2021). URL https://aip.scitation.org/doi/full/10.1063/5.0028951. Tex.ids= simbierowiczCharacterizingCryogenicAmplifiers2021a publisher: American Institute of Physics.

[25] Sorokin, P. P., Lasher, G. J. & Gelles, I. L. Cross Relaxation Studies in Diamond. *Physical Review* **118**, 939–945 (1960). URL https://link.aps.org/doi/10.1103/PhysRev.118.939.

[26] Ma, C. *et al.* Four-spin cross relaxation in a hybrid quantum device. *Physical Review A* **100**, 012322 (2019). URL https://link.aps.org/doi/10.1103/PhysRevA.100.012322.

[27] Zhang, G.-Q. *et al.* Exceptional Point and Cross-Relaxation Effect in a Hybrid Quantum System. *PRX Quantum* **2**, 020307 (2021). URL https://link.aps.org/doi/10.1103/PRXQuantum.2.020307. Publisher: American Physical Society.

[28] Baier, S. *et al.* Orbital and Spin Dynamics of Single Neutrally-Charged Nitrogen-Vacancy Centers in Diamond. *Physical Review Letters* **125**, 193601 (2020). URL https://link.aps.org/doi/10.1103/PhysRevLett.125.193601. Publisher: American Physical Society.

[29] Barson, M. S. J., Krausz, E., Manson, N. B. & Doherty, M. W. The fine structure of the neutral nitrogen-vacancy center in diamond. *Nanophotonics* **8**, 1985–1991 (2019). URL https://www.degruyter.com/document/doi/10.1515/nanoph-2019-0142/html. Publisher: De Gruyter.

[30] Isoya, J., Kanda, H. & Uchida, Y. EPR studies of interstitial Ni centers in synthetic diamond crystals. *Physical Review B* **42**, 9843 (1990). URL http://journals.aps.org/prb/abstract/10.1103/PhysRevB.42.9843.

[31] Kato, K., Sasaki, R., Matsuura, K., Usami, K. & Nakamura, Y. High-cooperativity cavity magnon-polariton using a high-Q dielectric resonator. *Journal of Applied Physics* **134**, 083901 (2023). URL https://doi.org/10.1063/5.0164545.

[32] Hamamoto, T., Bhunia, A., Bhattacharya, R. K., Takahashi, H. & Kubo, Y. Dielectric microwave resonator with large optical apertures for spin-based quantum devices. *Applied Physics Letters* **124**, 234001 (2024). URL https://doi.org/10.1063/5.0208113.

[33] Faramarzi, F. *et al.* A 4–8 GHz kinetic inductance traveling-wave parametric amplifier using four-wave mixing with near quantum-limited noise performance. *APL Quantum* **1**, 036107 (2024). URL https://doi.org/10.1063/5.0208110.

[34] Parker, D. J. *et al.* Degenerate Parametric Amplification via Three-Wave Mixing Using Kinetic Inductance. *Physical Review Applied* **17**, 034064 (2022). URL https://link.aps.org/doi/10.1103/PhysRevApplied.17.034064. Publisher: American Physical Society.

[35] Probst, S., Song, F. B., Bushev, P. A., Ustinov, A. V. & Weides, M. Efficient and robust analysis of complex scattering data under noise in microwave resonators. *Review of Scientific Instruments* **86**, 024706 (2015). URL http://aip.scitation.org/doi/10.1063/1.4907935.

[36] Walls, D. & Milburn, G. J. (eds) *Quantum Optics* (Springer, Berlin, Heidelberg, 2008). URL http://link.springer.com/10.1007/978-3-540-28574-8.

[37] Kubo, Y. *et al.* Strong Coupling of a Spin Ensemble to a Superconducting Resonator. *Physical Review Letters* **105**, 140502 (2010). URL http://link.aps.org/doi/10.1103/PhysRevLett.105.140502.

[38] Choi, H. & Englund, D. Ultrastrong magnetic light-matter interaction with cavity mode engineering. *Communications Physics* **6**, 1–9 (2023). URL https://www.nature.com/articles/s42005-023-01224-x. Number: 1 Publisher: Nature Publishing Group.

[39] Collett, M. J. & Gardiner, C. W. Squeezing of intracavity and traveling-wave light fields produced in parametric amplification. *Physical Review A* **30**, 1386–1391 (1984). URL https://link.aps.org/doi/10.1103/PhysRevA.30.1386. Publisher: American Physical Society.

[40] Diniz, I. *et al.* Strongly coupling a cavity to inhomogeneous ensembles of emitters: Potential for long-lived solid-state quantum memories. *Physical Review A* **84** (2011). URL http://link.aps.org/doi/10.1103/PhysRevA.84.063810.

[41] Kurucz, Z., Wesenberg, J. H. & Mølmer, K. Spectroscopic properties of inhomogeneously broadened spin ensembles in a cavity. *Physical Review A* **83** (2011). URL http://link.aps.org/doi/10.1103/PhysRevA.83.053852.

[42] Julsgaard, B. & Mølmer, K. Dynamical evolution of an inverted spin ensemble in a cavity: Inhomogeneous broadening as a stabilizing mechanism. *Physical Review A* **86**, 063810 (2012). URL http://link.aps.org/doi/10.1103/PhysRevA.86.063810.

[43] Carmichael, H. J. *Statistical Methods in Quantum Optics 1: Master Equations and Fokker-Planck Equations* (Springer Science & Business Media, 2013). Google-Books-ID: 5hv2CAAAQBAJ.

Supplementary Files

This is a list of supplementary files associated with this preprint. Click to download.

- Supplementary.pdf